

Fischer, R., Schoeller, J., Rossi, R. M., Derome, D., & Carmeliet, J. (2022).
wicking fingering in electrospun membranes. *Soft Matter*, 18(30), 5662–5675.
<https://doi.org/10.1039/d2sm00472k>

Wicking fingering in electrospun membranes

Robert Fischer^{1,2,3}, Jean Schoeller², René M. Rossi², Dominique Derome⁵, and Jan Carmeliet³

¹Laboratory of Multiscale Studies in Building Physics, Empa, Swiss Federal Laboratories for Materials Science and Technology, Überlandstrasse 129, 8600 Dübendorf, Switzerland

²Laboratory for Biomimetic Membranes and Textiles, Empa, Swiss Federal Laboratories for Materials Science and Technology, Lerchenfeldstrasse 5, 9014 St. Gallen, Switzerland

³Chair of Building Physics, Swiss Federal Institute of Technology Zürich (ETHZ), Stefano-Franscini-Platz 5, 8093 Zürich, Switzerland

⁴Swiss Light Source, Paul Scherrer Institut, 5232 Villigen PSI, Switzerland

⁵Department of Civil and Building Engineering, Université de Sherbrooke, J1K 2R1 Sherbrooke, Canada

August 15, 2022

Abstract

Pronounced fingering of the waterfront is observed for in-plane wicking in thin, aligned electrospun fibrous membranes. We hypothesize that a perturbation in capillary pressure triggers the onset of fingering, which grows in a non-local manner based on the waterfront gradient. Vertical and horizontal wicking in thin electrospun membranes of poly(ethylene-*co*-vinyl alcohol) (EVOH) fibers with varying fiber alignment and degree of orientation is studied with backlight photography. A non-local transport model considering the gradient of the waterfront is developed, where fiber orientation is modeled with a correlated random field. The model shows that a transition from straight to highly fingered waterfront occurs during water uptake as observed in the experiment. The size and shape of the fingers depend on fiber orientation. Based on good model agreement, we show that, during wicking in thin electrospun membranes, fingering is initially triggered by a perturbation in capillary pressure caused by the underlying anisotropic and heterogeneous membrane structure which grows in a non-local manner depending on the waterfront gradient.

1 Introduction

Electrospun nanofibrous membranes (ENM) are soft materials with promising biomedical applications as scaffolds for tissue engineering [1, 2], advanced wound dressing [3, 4] or drug delivery [5, 6]. Electrospun membranes show furthermore potential in filtration [7, 8], as waterproof, yet vapor open, textiles [9, 10, 11] and gas diffusion layer in fuel cells [12, 13].

Wicking is the spontaneous uptake of a wetting liquid into a porous medium by replacing a non-wetting fluid. Unlike classic porous media such as sedimentary rock, where liquid interfaces navigate into a network of pore bodies, during wicking in ENM a film with continuous waterfront develops, stretching between and over many fibers [14]. Attention has been paid to water transport normal to the ENM-plane [9, 10, 11], but not much to in-plane transport. An extended overview of experimental methods to study wicking in primarily fibrous porous media is given by [15]. Experimentally studying wicking has traditionally been done by tracking the waterfront with optical methods [15]. Such methods work best for flat and fairly transparent materials with saturated piston-like uptake, i.e. without strongly varying moisture content upstream of the waterfront. Wicking is a macroscopic phenomenon that is determined by water/air/solid interactions at pore scale. Experimental techniques at pore scale, like X-ray tomographic microscopy (XTM) have become a popular tool to obtain 3D images of real porous structures [16]. However, XTM has yet to have the required spatial resolution to capture adequately ENM systems [17], and thus is not able to resolve the inter-fiber void structure of ENM, nor the imaging

of the water filling process of these voids. Scanning electron microscopy (SEM) readily achieves a spatial resolution of few nanometers even for large samples and, under low vacuum atmosphere, requires little to no sample preparation. Although SEM can only access the sample surface, the approach provides useful information when the surface is representative for the bulk of the porous medium. Further, environmental (E)SEM under water vapor atmosphere allows to a certain extent the observation of liquid water along the fibrous structure. As a result, the optical method of backlight photography is the main method of investigation at hand to study wicking in ENM.

Pore network models (PNM) are widely used to study flow in heterogeneous porous media [18, 19, 20, 21]. The challenge for the applicability of PNM lays in the necessary set of pore information, i.e. the capillary pressure in two-phase pores and the throat conductivity. The translation of the notion of pores to ENM is difficult because liquid menisci are not confined locally to pore bodies, but are rather stretched between and over several fibers. ENM are not networks of connected pores and throats, but rather porous media with low solid fraction and local heterogeneity. Continuum models are able to include such local heterogeneity by varying flow properties on the material domain [22, 23], but cannot capture the far-range influence of distorted liquid interfaces. Lattice-Boltzmann-Method (LBM) is a popular direct numeric method that captures two-phase phenomena, but is still too computationally costly to resolve the exact geometry of ENM on fiber scale. The implementation of sub-resolution processes, e.g. contact angle hysteresis on rough surfaces [24, 25], is an ongoing challenge for coarse-grain-like models. Theoretical and experimental works on hysteresis and wetting of rough surfaces often discuss the superposition of different effects, e.g. surface wetting and volume restriction for droplet deposition[26]. In other cases, curved water-interfaces and an apparent contact angle equal to Young’s angle are assumed to derive the capillary pressure for uptake from an unlimited reservoir[27], while it can be shown, that wicking is a free energy minimization process[28, 29] where the work is provided by wetting hydrophilic surfaces. Thus, there is research need for an alternative modeling approach or a modification of current models to capture the intriguing phenomenon that is wicking in ENM.

This study discusses in-plane water wicking in thin electrospun membranes of poly(ethylene-*co*-vinyl alcohol) (EVOH) fibers. The process is experimentally documented with backlight photography. After an initial period of a straight waterfront, a transition to pronounced fingering is observed which is not yet explained. ESEM helps to understand the underlying interaction of water with the fibrous structure. Finally, a numerical model is developed that recovers the characteristic wicking dynamics of water in electrospun EVOH membranes.

2 Materials and methods

2.1 EVOH membranes

A solution of 12% poly(ethylene-*co*-vinyl alcohol) (EVOH, Soarnol A4412, Nippon Gohsei, Japan) dissolved in hexafluoroisopropanol (Sigma Aldrich) (HFIP):water (3:1) is electrospun for 4h at $10\mu\text{l}/\text{min}$, under a potential difference of 22 kV (+16 -6kV) and a distance from spinneret to collector of 25 cm. The fiber are collected on a 250x250 mm aluminum foil wound around a rotating drum. The drum rotation velocity is varied from 500, 1000, 1500 to 2000 rpm to induce different degrees of fiber orientation [30]. The membranes are then left to dry overnight in a vacuum oven. The membrane thickness is measured to be $30\mu\text{m}$ using X-ray tomographic microscopy for one small sample taken at the the center of one membrane and estimated to be comparable in all other cases as the same deposition process was used. Samples of $60\times 30\text{ mm}^2$ are cut with razor blades, with the longer side either parallel or normal to the principal fiber orientation. An adhesive aluminum tape is glued around the short sides of the samples and carefully flattened to seal the membrane at these ends. Small fishing weights are attached to one of the aluminum tapes to straighten the membrane without stretching the sample when hanged into the setup for the vertical wicking experiment.

2.2 Environmental scanning electron microscopy

Scanning electron microscopy (SEM) is employed to characterize each prepared membrane with one small sample for each set drum rotation, and consequentially degree of fiber alignment. Without any further preparation, the sample is laid flat on the sample stage of a scanning electron microscope (Thermo Fisher Scientific Quanta 650 FEG). The chamber pressure is set to 70 Pa of water vapor pressure in low vacuum mode and microscopic images are acquired at 2000x magnification. The fiber orientation is then analyzed with the OrientationJ-plugin [31] for Fiji/ImageJ [32] using a size of 2 pixels for the structure tensor

corresponding to the thickness of the thinner fibers and cubic splines to calculate the image gradient. The interaction of water with the fibrous structure is investigated by "Environmental"-SEM (ESEM), allowing higher water vapour pressure. A paperclip that acts as a support for a small strip of ENM is clamped on a metallic sample holder in the shape of a small bucket. One end of the strip hangs in the sample holder. The setup is placed on a Peltier stage and cooled to -3°C . When increasing the water vapor pressure to 700 Pa, water condensates in the sample holder and acts as a reservoir in contact with the membrane, allowing the onset of horizontal wicking in the ENM-strip. This method allows the acquisition of microscopic images at the surface of the ENM during water wicking.

2.3 Backlight photography

Backlight photography exploits the change in material transparency when the material becomes wet. The thin membranes are ideal for backlight photography due to their diffusive transparency to visible light. The sample holder in figure 1 consists of a rack with a slit cross-piece that allows to hang the prepared membrane samples with two binder clips, while weights at their base keep the sample in the vertical plane. The lowest millimeters of the membrane sample reach below the edge of a rectangular container that acts as water reservoir. The reservoir is connected through a tube to a water canister. By lifting or lowering the canister, the water level inside the reservoir can be adjusted by hydraulic equilibration.

The sample holder is placed in front of a commercial camera (Nikon D90) that is connected to a personal computer for remote control and image acquisition. The sample is illuminated from the back side by an array of LEDs which light is diffused by a milky plastic sheet (figure 1).

Before each sample acquisition, the focal length of the camera objective (Nikkor Micro 60mm 1:2.8 G) is adjusted and after the acquisition, a picture of a reference calibration plate is taken at the same focal spot as reference yielding the pixel size. The camera settings aperture, illumination time and sensor sensitivity (ISO) are adjusted once for a wet test sample and kept constant throughout the experiment for all samples.

This experimental protocol is followed for all samples: image acquisition is started with one frame every two seconds. After taking a few frames, the water canister is manually lifted about one meter above the experimental stage to provoke fast inflow into the reservoir. Once the water level reaches the upper edge of the reservoir, the canister is placed on a prepared platform to keep the water at this set level. This procedure ensures that wicking in all submerged samples occurs under identical starting conditions, i.e. at a constant water level. Small variations in timing are corrected in the image analysis by calibrating $t = 0$ at the appearance of the waterfront in the field of view of the camera. After 10 minutes, the acquisition frequency is reduced to one frame every five seconds and continued for another 25 minutes. Finally, the reservoir is drained and the sample removed.

The horizontal wicking experiment is performed in a slightly modified setup to study wicking without the influence of gravity. A thin metal rod is placed across the reservoir to hang a small part into the reservoir, while the sample is held horizontally. Camera and light source are rearranged to allow the same experimental procedure. Experiments are performed in a room with controlled ambient conditions at 37% relative humidity and 23°C . Given the fragility of the samples, each experiment uses a new sample and no sample is reused.

2.4 Image processing

Digital image processing is performed using a Python script employing the standard libraries NumPy, SciKit-image and Joblib. All frames are cropped to exclude the edge of the sample patches, the upper part of the sample that remained dry until the end of the acquisition and the lower section where the image is distorted by a thick capillary bridge between sample and the water surface in the reservoir (shadowy zone at the bottom of figures 8). The file timestamp gives the corresponding physical time of the frame, which is then manually calibrated for each sample to determine the onset of uptake at $t = 0$. Water-wetted parts of the membrane appear clearly brighter than the dry part (figure 8). The rgb-image data is converted to grayscale according to cathode ray tube (CRT) phosphor weighting ($Gray = 0.2125Red + 0.7154Green + 0.0721Blue$). A grayscale threshold is chosen manually for every sample, to convert the image data into a binary matrix of wet and dry pixels. The waterfront position $y(x, t)$ is extracted by counting the height of the pixels per column. The mean waterfront position is calculated as $\langle y(t) \rangle_x$, where the front maximum and minimum are the respective profile extremes. The waterfront



Figure 1: Experimental setup for backlight photography.

length is calculated by adding up the distances between the front pixels of every column k , i.e.

$$p = \sum_k \sqrt{[y(x_{k+1}) - y(x_k)]^2 + [x_{k+1} - x_k]^2} \quad (1)$$

where the spacing between columns $(x_{k+1} - x_k)$ is one pixel. The waterfront length is converted to SI units (meter) knowing the pixel size. The pixel size is determined and considered in the processing for each sample separately with the optical calibration plate. The average pixel size is $9.97 \mu\text{m}$, with $9.39 \mu\text{m}$ and $10.07 \mu\text{m}$ as found minimum and maximum. The pixels are squares with equal lengths in both directions.

2.5 Theory

Bell, Cameron[33], Lucas[34] and Washburn[35] developed a one-dimensional model describing wicking in porous media as capillary rise in a cylindrical tube governed by the balance of capillary pressure p_c , hydrostatic pressure due to gravity p_g and pressure drop due to viscous dissipation p_v (equation 2a). In most cases, turbulent effects are negligible because wicking is slow as displayed by small Reynolds numbers. The solution of the differential equation 2b disregarding the short initial inertial phase occurring in some combinations of liquids and porous media[36] is given by equation 2c [34]:

$$p_c = p_g + p_v \quad (2a)$$

$$\rho g h_0 = \rho g h + \hat{R} A h \frac{dh}{dt} \quad (2b)$$

$$\ln \left(\frac{h_0 - h}{h} \right) + \frac{h}{h_0} = -\frac{K t}{h_0} \quad (2c)$$

$$K = \frac{\rho g}{\hat{R} A} \quad (2d)$$

where $\rho \left[\frac{\text{kg}}{\text{m}^3} \right]$ is the liquid density, $g \left[\frac{\text{N}}{\text{kg}} \right]$ the gravitational acceleration and $h_0 \text{ [m]}$ the maximal uptake height when $\frac{dh}{dt} = 0$ (equation 2b), $h = h(t)$ is the current wicking height, $R = \hat{R} h$ the flow resistance for the momentary h , $\hat{R} \left[\frac{\text{Pas}}{\text{m}^4} \right]$ a distance specific resistance factor and $A \text{ [m}^2\text{]}$ the cross-section area of the pore space. Initially, for $h \ll h_0$, gravity can be neglected and the uptake dynamics reduces to Washburn's square root of time law:

$$h(t) = \sqrt{2K h_0 t} = C \sqrt{t} \quad (3)$$

The parameters $K \left[\frac{\text{m}}{\text{s}} \right]$, $h_0 \text{ [m]}$ and $C \left[\sqrt{\frac{\text{m}}{\text{s}}} \right]$ are accessible from uptake experiments measuring $h(t)$, where C is the initial slope of the uptake versus square root of time, h_0 the maximum uptake height and $K = \frac{C^2}{2h_0}$. For a cylindrical tube, C is given as [35]

$$C = \sqrt{\frac{\gamma r \cos \vartheta}{2\eta}} \quad (4)$$

where $\gamma \left[\frac{N}{m} \right]$ is the surface tension of water in air, $\vartheta [^\circ]$ Young's contact angle, $\eta [Pa \cdot s]$ the dynamic viscosity of the liquid and $r [m]$ the tube, i.e. pore radius. This model can be applied to wicking under the condition that the water front moves uniformly in porous media, i.e. $h(x, t) \approx h(t)$. This is not always the case, like demonstrated in [37, 38, 39] showing that the fluid interface can show quite distinct shapes under forced flow conditions, such as capillary and viscous fingering. Another wetting process showing fingering is the runoff of a thin film, where the onset of fingering is found to a surface tension induced instability [40, 41]. While showing similarities, the mechanisms at play in capillary and thin-film fingering cannot explain wicking fingering in ENM. Capillary fingering follows percolation paths induced by pore geometry while the millimeter wide fingers in ENM are much larger than the underlying pore structure with micrometer wide inter-fiber voids. Thin film fingering during runoff develops from modes of the liquid-air interface while fingering in ENM happens inside a porous medium with water/fiber/air interfaces. In the following, we develop a model describing fingering occurring during wicking in ENM. The capillary pressure is defined as the change of free energy dF per unit volume dV (equation 5), which can be determined by the change of interface area water-air dA_{wa} and wetted solid surface area dA_{ws} .

$$p_c = -\frac{dF}{dV} = -\frac{\gamma (dA_{wa} - \cos \vartheta dA_{ws})}{dV} \quad (5)$$

Given the small membrane thickness, we approximate the problem to be two dimensional assuming translational symmetry ($\frac{\partial p}{\partial z} = 0$, $\frac{\partial q}{\partial z} = 0$, $\frac{\partial K}{\partial z} = 0$) with the z -axis in the direction normal to the membrane plane. Then, the change of water-air interface area equals the change in thin water film area sticking on the two faces of the membrane

$$dA_{wa} = 2dsdh \quad (6)$$

where ds is the length of the water front in the unit volume dV and dh the movement of the water front. The change of wetted solid surface is written as

$$dA_{ws} = \alpha dsdh \quad (7)$$

where α is a scaling factor describing the specific fiber surface area wetted when advancing the water front by dh . When the water front is a straight line, $ds = ds_0$. When the water front is non-linear, the length is described introducing a factor $l_s \geq 1$ (figure 2)

$$ds = l_s ds_0 \quad (8)$$

where l_s equals the gradient of the water front with respect to infinitesimal short ds_0 , or

$$ds = \frac{\partial s}{\partial s_0} ds_0 \quad (9)$$

Introducing (6), (7) and (8) into equation (5), we get

$$p_c = -\frac{\gamma (2 - \alpha \cos \vartheta) l_s ds_0 dh}{dV} \quad (10a)$$

$$dV = b ds_0 dh \quad (10b)$$

$$p_c = -\frac{\gamma (2 - \alpha \cos \vartheta) l_s}{b} = p_{c0} l_s \quad (10c)$$

where the volume dV is described by the product of water front movement dh , the membrane thickness b and straight horizontal baseline ds_0 (equation 10b). The capillary pressure at a given location of the water front is found to be equal to the capillary pressure p_{c0} for a straight water front times a factor l_s equal to the gradient to the non-linear water front. p_{c0} is mostly determined by the specific surface area related to α . EVOH exhibits partial wetting with a contact angle typically around 50° . An exact contact angle measurement is currently not attainable for the actual sub-micrometer electrospun fibers. However, $\cos \vartheta$ only varies little for $50^\circ \pm \Delta \vartheta$. This means that when fingering is initiated and the water front is non-linear, the factor $l_s > 1$. During fingering, the free energy rate and capillary pressure increase when the water front evolves from a straight front to a non-linear one. Since the water front is initially straight fingering needs to be triggered by a small perturbation in capillary pressure by the underlying heterogeneous fiber structure of the membrane. At that moment, the perturbation can grow into a finger by non-locally increasing the capillary pressure. We note that the factor l_s is not a constant but depends on the local gradient of the water front which depends on the finger shape (figure 2).

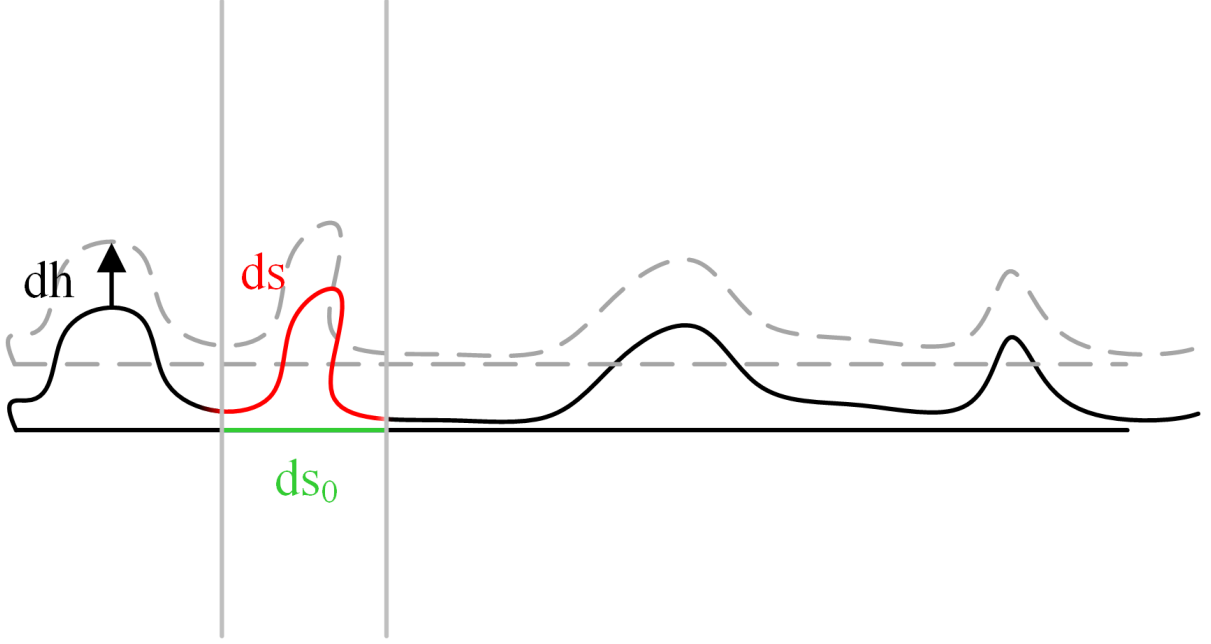


Figure 2: Schematic representation of lengthened waterfront for perturbed waterfront.

2.6 Model

For modeling wicking two approaches at two different scales can be considered. The first approach is a discrete approach at fiber scale, where fibers with sub-micrometer radii form a complex mesh in a thin membrane with a thickness of around $30 \mu\text{m}$. Computational costs make direct simulation of wicking in this fibrous structure unfeasible. The second approach considers that, during the uptake, water rises up to several millimeters, after which it forms fingers, which are several millimeters wide reaching up to a height of around 30 mm . At this mm-scale the membrane may be considered as a macroscopic continuum and wicking can be modeled as a 2D flow process. The length dimensions are obtained from the experiments presented below. To mathematically describe the wicking process, we follow a control volume technique, where the membrane is divided into a 2D regular grid of square elements with equal size Δ . The flow between grid neighboring elements is described by:

$$q_{ij} = A_{ij} g_{ij} (p_j - p_i) \quad (11)$$

where g_{ij} is the conductivity between two nodes described below and p_i and p_j are the pressures within the nodes. A_{ij} is the adjacency matrix which is one for neighboring pairs, $\frac{1}{\sqrt{2}}$ for diagonal neighbors taking into account their longer diagonal distance, and zero anywhere else (figure 3). The pressure in the water-filled domain is solved applying conservation of mass

$$0 = \sum_j q_{ij} \quad (12)$$

As boundary conditions of the water-filled domain, zero inlet pressures ($p_i = 0$) are prescribed at the base of the domain while at the waterfront the prescribed pressures are $p_{ci} - \rho g y_i$, where y_i is the height of the element to consider gravity and p_{ci} the capillary pressure. Using equation (11) and (12), the effective flow in the elements at the front can be calculated for each time step and their degree of saturation s_i can be updated as

$$s_i(t) = s_i(t - \Delta t) + \frac{q_i(t)}{v_0} \Delta t \quad (13)$$

where $v_0 = b\Delta^2$ is the element volume. Once s_i reaches a degree of saturation close to one ($s_i \geq 0.98$), the element i is considered filled, removed from the front and its non-wetted neighboring elements are added to the waterfront.

The grid conductivity $g_{ij} \left[\frac{\text{m}^3}{\text{Pas}} \right]$ is

$$g_{ij} = \frac{C^2 b}{\rho g h_0 (s_i + s_j)} \frac{1}{1 + \sqrt{2}} \quad (14)$$

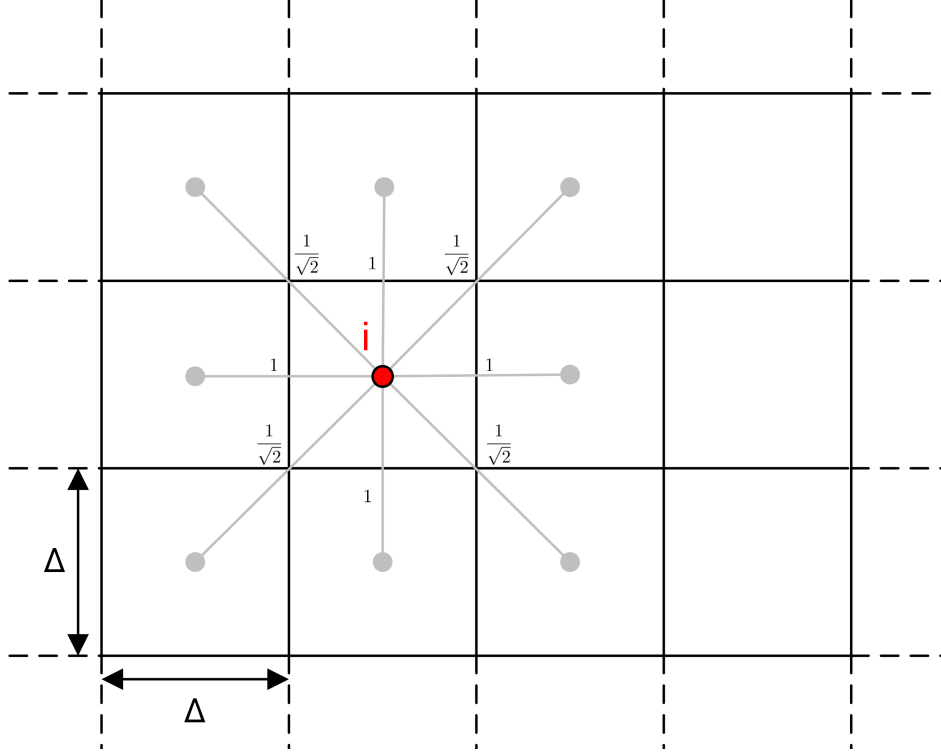


Figure 3: Schematic representation of the model grid. An element i is connected to its neighbors where the distance gives the value in the adjacency matrix to scale the conductivity g_{ij} .

The factor $\frac{1}{1+\sqrt{2}}$ scales the combined conductivity of diagonal and straight element connections (see equations 11 and 12) to be in correct relation with the Lucas-Washburn model (equation 3). The derivation can be found in the appendix (section A.1). The parameters h_0 and C , respectively the maximal uptake height and the initial slope of the uptake curve versus square-root of time (see equation 3), are determined from the experiment. The model calculates the filling state of the grid elements and provides the waterfront position based on the grid size Δ . At the heart of the model is the calculation of the waterfront capillary pressure p_{ci} with equation (10c). For the control volume, the length of a straight waterfront equals the element size, or $ds_0 = \Delta$. When the waterfront is non-linear, the factor l_s in equation (10c) has to be determined. A continuous waterfront is derived from the rugged grid element front by smoothing the y_i coordinates of the waterfront elements with a Gaussian filter (σ_a). In a next step, the coordinate pairs (x'_i, y'_i) at the waterfront are determined where y'_i is the maximum y_i at $x_i = x'_i$ for a certain element column. These pairs of coordinates are considered to sufficiently approximate the smooth waterfront. Δx_i and Δy_i are calculated as second order accurate central differences of x'_i and y'_i respectively. The in the model implemented waterfront length has counts of elements as unit and consequently the dimensionless factor l_{si} per element is then

$$\Delta x_i = \frac{x'_{i+1} - x'_{i-1}}{2} \quad (15a)$$

$$\Delta y_i = \frac{y'_{i+1} - y'_{i-1}}{2} \quad (15b)$$

$$l_{si} = \sqrt{(\Delta x_i)^2 + (\Delta y_i)^2} \quad (15c)$$

In a next step, l_{si} is smoothed with a Gaussian filter (σ_c) and remapped to the front coordinates (x_i, y_i) from the nearest coordinate pair (x'_i, y'_i) .

To trigger finger formation, a perturbation in capillary pressure is added based on the underlying membrane anisotropic and heterogeneous fiber structure. Heterogeneity is modelled by a random field adding spatially correlated noise to a chosen constant capillary pressure p_{c0} in each element. This perturbation in the capillary pressure is motivated by small variances in the fibrous structure and available fiber surface at sub-micron fiber scale. Due to fiber alignment, the random field of p_{c0} will show an anisotropic spatial correlation, i.e. p_{c0} varies less in fiber orientation than in the direction normal to fiber direc-

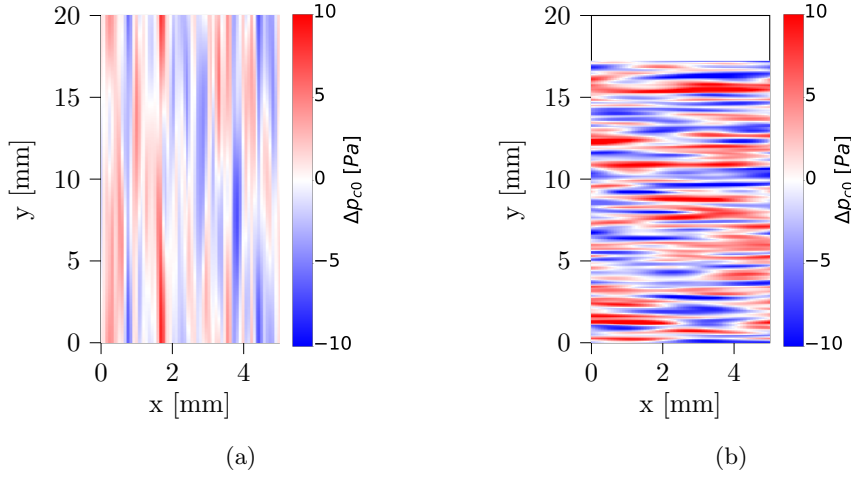


Figure 4: p_{c0} random field for wicking in a) fiber direction and b) normal direction. The color gradient denotes the deviation from the mean capillary pressure of the grid element.

tion. While this assumption is reasonable and the SEM images confirm an anisotropic image correlation in fiber orientation, i.e. fiber alignment, (figure 6), taking in account this assumption in the model is not straightforward. We model the random field by first assigning a random perturbation to each grid element

$$p_{c0i} = p_{c0} (1 + \Delta_p N) \quad (16)$$

where Δ_p is a noise factor and N a random number between -0.5 and 0.5. In a next step, the obtained and uncorrelated random field is transformed into an anisotropic correlated random field using a two-dimensional Gaussian filter with different correlation lengths in x- and y-direction, σ_x and σ_y to reflect the fiber alignment in the membrane, as shown in figure 4. We note that the color contrast in figure 4b is stronger because the long image correlation length σ in fiber direction is effective beyond the lateral domain dimension leading to more pronounced smoothing in figure 4a. As shown in the later model analysis, we can accept this discrepancy as it has negligible influence.

3 Experimental results

3.1 Scanning Electron Microscopy

3.1.1 fiber orientation

Figure 5 shows the obtained SEM-images of the ENM samples. They reveal an open pore structure with low solid fraction, i.e. the membranes show a high porosity. The fiber orientation distributions obtained from the SEM-images for the different samples are presented in figure 6a. Due to the collector drum rotation, all samples show a preferred fiber orientation in the direction of the drum rotation (0°). While there is a notable probability to find fibers to be orientated in all directions for slow drum rotation (500 rpm), the probability that fibers are oriented at more than $\pm 45^\circ$ from the drum rotation plane is clearly reduced for higher rotation speeds. Also, the distribution becomes higher and narrower, centered around 0° for higher rotation speeds. A measure for the fiber alignment, called degree of orientation, is defined as the standard deviation σ obtained from fitting a normal distribution to the orientation distribution. With increasing drum rotation, the fibers in the ENM are more aligned as shown by the decrease of the alignment value in figure 6b. Apart from the degree of fiber orientation, no substantial differences in thickness, contact points and inter-fiber spacing are observed across the membranes.

3.1.2 water-fiber interaction

Figure 7 contains an ESEM-image of the zone between dry and wet ENM. The waterfront is indicated by fibers lighted up (white zone), while the part left of the waterfront is more grayish showing that water fills the membrane submerging the fibers in water. The waterfront boundary shows overall a smooth line on large scale ($\approx 100 \mu m$), but a short-range wavy pattern is present at smaller scale ($\approx 10 \mu m$).

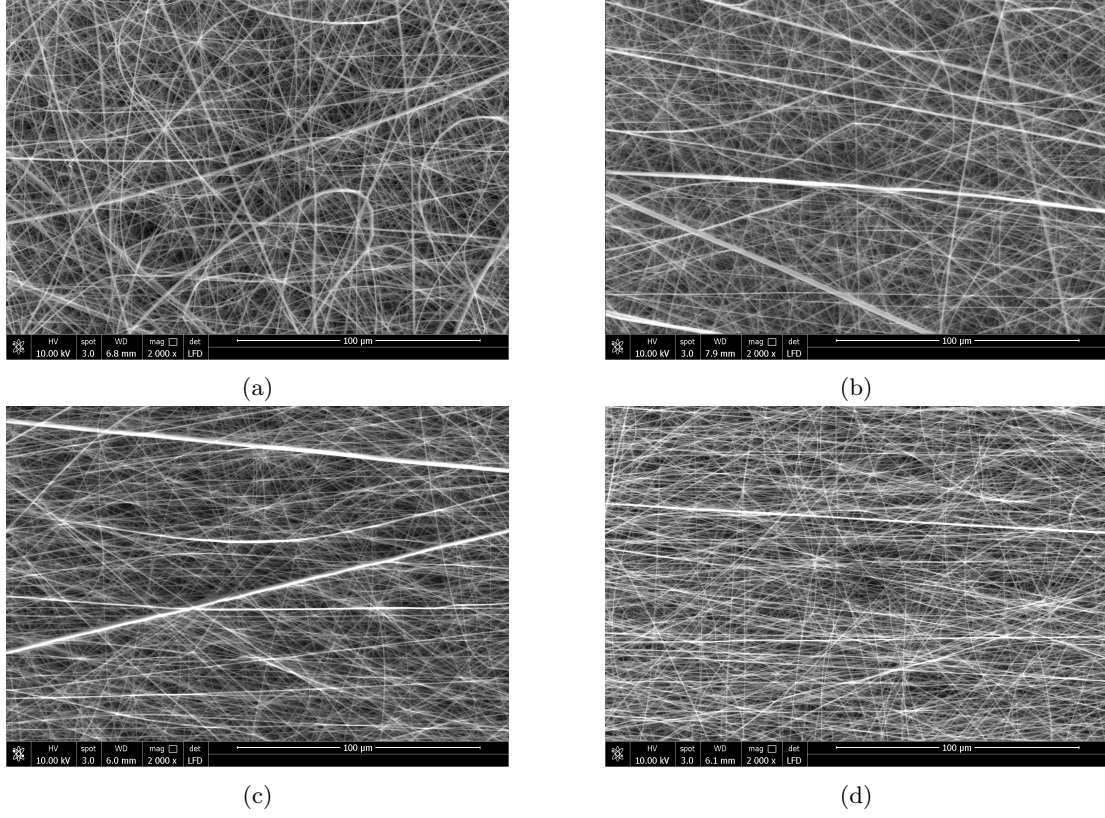
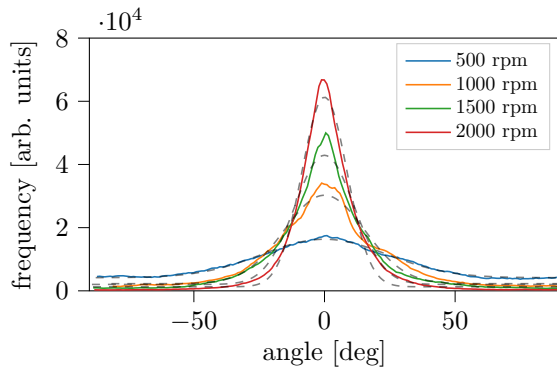
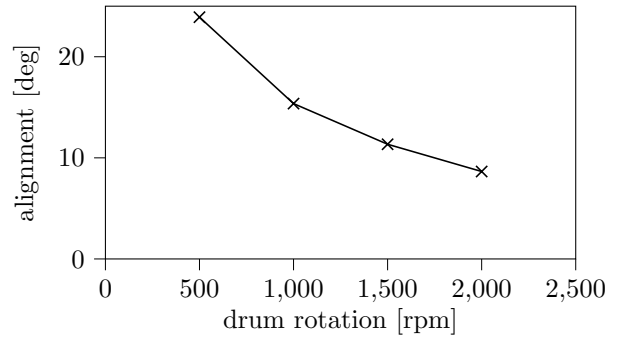


Figure 5: Scanning electron microscopy of ENM prepared with a) 500 rpm, b) 1000 rpm, c) 1500 rpm and d) 2000 rpm drum rotation speed.



(a)



(b)

Figure 6: Fiber orientation statistics for membranes prepared at different collector drum rotation speeds. a) distribution of fiber orientation from SEM with fitted Gaussian (dashed) and b) obtained Gaussian- σ as orientation variance

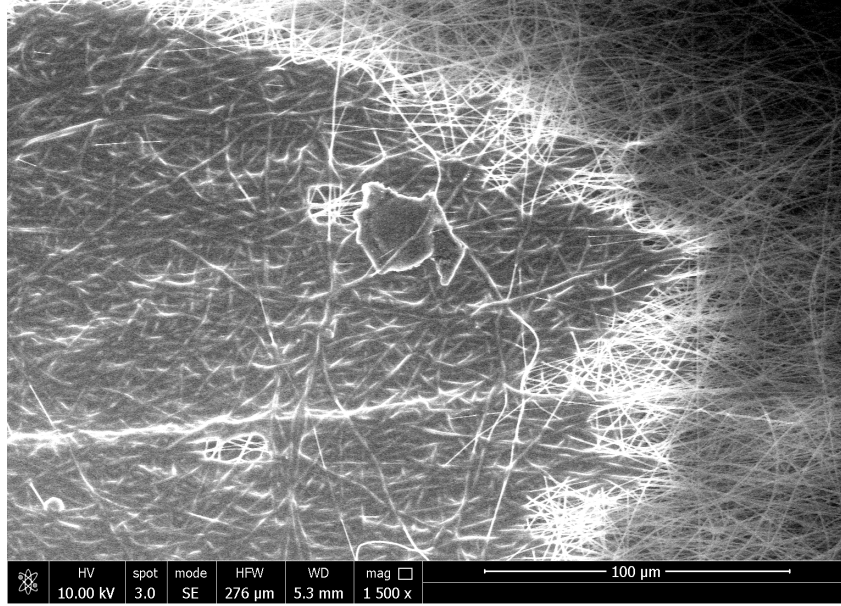


Figure 7: ESEM image of ENM at the boundary between wet (left) and dry (right) zones. Red frames mark zones of interrupted surface film for a view into the bulk layers of the membrane.

Further, liquid bridges span directly at fiber scale ($\approx 1 \mu\text{m}$). Overall, the waterfront appears as a smeared interface zone consisting of a collection of wetted fibers forming a rather continuous front shape at larger scale, and quite independent from the fiber scale pattern. This waterfront pattern is very different to the waterfront in classic porous media where the front is a liquid meniscus spanning well-defined pore bodies.

3.2 Backlight Photography

Figure 8 shows a series of raw images for different samples obtained by backlight photography showing the vertical wicking along fiber orientation (figure 8 a-f), the vertical wicking normal to fiber orientation (figure 8 g-k) and the horizontal wicking along fiber orientation (figure 8 l-o). Vertical wicking along fiber direction shows initially a rather uniform waterfront (figure 8c), then thin spikes appear (figure 8d) that grow in length forming fingers (figure 8e) before they reach a maximal height, after which they thicken laterally forming a broccoli shape (figure 8f). For vertical wicking normal to fiber direction, fingers appear at a similar time (figure 8d and h), but they tend to grow laterally (figure 8h) and i), resulting in a rather wavy waterfront because the small initial horizontal spikes are caught by the main waterfront. Horizontal wicking in fiber direction undergoes comparable behavior to the vertical rise, as it also leads to formation of parallel fingers. Due to the horizontal test setup, a large angular water bridge forms below the horizontal membrane as seen by the large dark area at the bottom of the images (figure 8m-o).

The wicking height over time is used to describe the wicking dynamics. As a result of the necessary cropping of the images (see red frames in figure 8), early uptake and a part of the stage with a stable waterfront cannot be considered (figure 8b). The front height is determined as the average waterfront position across the width of the sample. Figure 9 shows the mean height versus time for wicking along and normal to the fiber orientation. All curves show two parts: a first experimentally apparently linear part, followed by a second period where the maximum height is slowly attained. However upon closer examination, the early phase ($t < 150 \text{ s}$) can be fitted to a square-root of time behavior (equation 3) providing the wicking constant C used later as model input (table 1). Deriving a hydraulic radius r from C would give a value of 6 nm (equation 4) which magnitude has no relation to the actual membrane structure. The uptake is much slower than predicted by Washburn's law (equation 4, blue curves in figure 9), when using the mean fiber distance as pore size (around $1 \mu\text{m}$). This indicates that the wicking process cannot be considered as a classical pore filling process, but rather as a flow along the fibers, forming a thin film at the two sides of the thin fibrous membrane and so filling the porous space at the same time. In the cases of wicking in fiber direction (black curves in figure 9), the maximum height for $t > 1400 \text{ s}$ is about 20 mm and independent of the drum rotation (degree of fiber orientation). In the

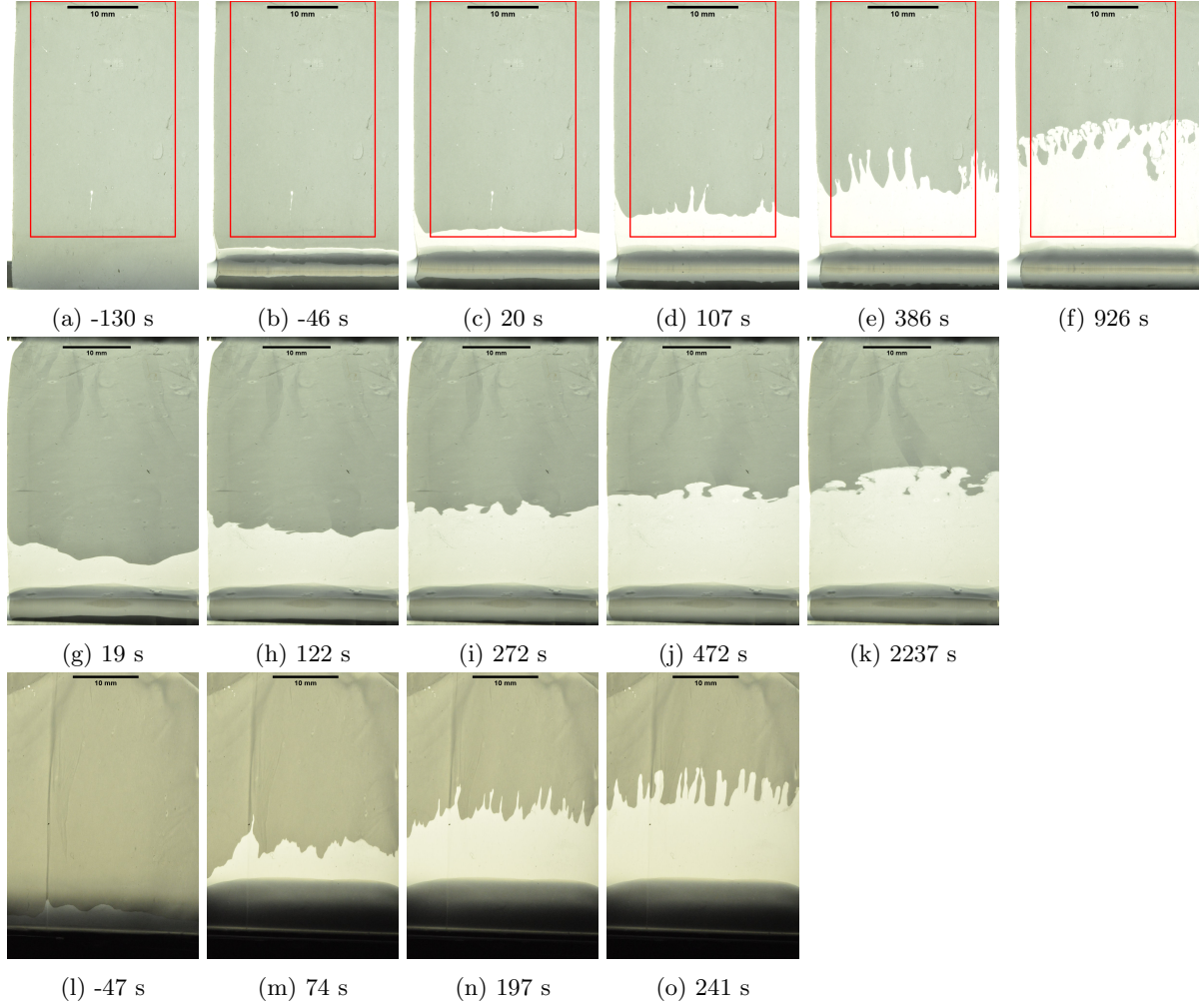


Figure 8: First row a-f: vertical uptake along fiber orientation of 1000 rpm membrane, the red frame shows how the cropping is done; second row g-k: vertical uptake normal to fiber orientation of 1500 rpm membrane; third row l-o: horizontal uptake along fiber orientation of 1500 rpm membrane, time calibrated for images taken before and after water enters the cropping frame.

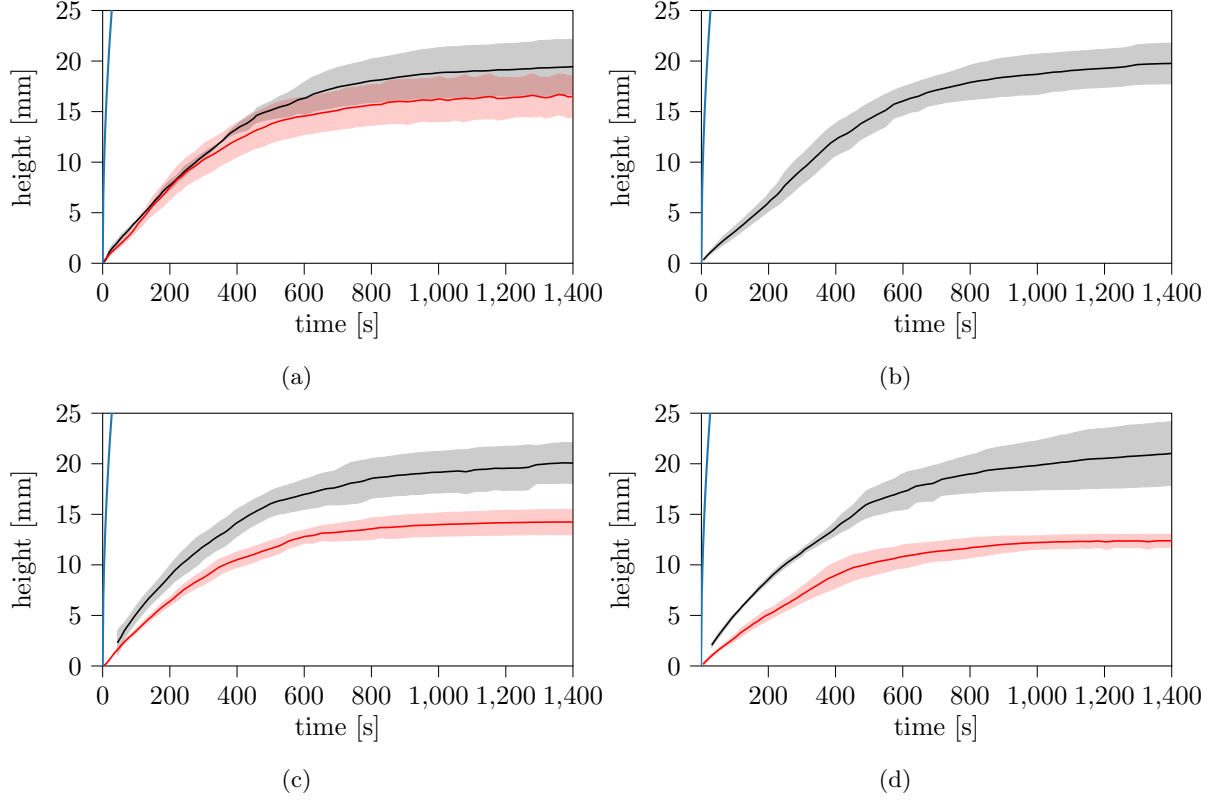


Figure 9: Average height (solid line) and standard deviation (light area) over time for samples taken from membranes produced with drum rotation a) 500 rpm, b) 1000 rpm, c) 1500 rpm and d) 2000 rpm. Black - fibers oriented along wicking direction; red - normal to wicking direction; blue - Washburn for $r = 1 \mu m$

cases of wicking normal to the fiber orientation (red curves in figure 9), the initial flow rate and maximum height decrease with increasing drum rotation. We note that wicking on 1000 rpm membrane is missing because too much material of the small membrane patches has been used for testing the experimental setup. For wicking in the horizontal plane, thus without the influence of gravity, and along the fiber orientation, the wicking front shape is qualitatively equivalent to vertical wicking (figure 8). The same membranes are tested in horizontal and vertical wicking as shown in figure 10a and no difference in uptake behavior is observed. The fingers are very similar and the uptake flattens out after about 500 s. In contrast to the Lucas-Washburn model (equation 2) where the maximum height is due to the balance of capillary force and gravity, gravity apparently does not play a role in the wicking process in ENM. Since we have a film at both sides of the membrane, evaporation may play an important role and might finally stop the uptake process, when the inflow equals the evaporation rate. To get an estimate of the evaporation rate, a small dish filled with water is placed on a micro-balance and its mass loss over time recorded. We remark that the evaporation rate from the membrane itself during wicking can be different, due to a different local mass transfer coefficient or due to the heat produced by the lamp. The measured evaporation rate per area is multiplied twice with the wet membrane area at a given time to account for both sides of the membrane. When the waterfront advances, additional water surface can undergo evaporation leading to increasing evaporation losses. The cross-section of the wicking flow in the membrane remains constant while the waterfront advance becomes slower leading to decreasing wicking flux and consequently to lower water volume flux from the reservoir. We observe a crossover of the evaporation losses compared to the effective wicking uptake at around 400 s (figure 10b), which matches roughly the onset of the flattening of the uptake curve. This means that the maximal wicking height is limited by evaporation and not by gravity. Figure 11 illustrates the evolution of the waterfront length over time as average per drum rotation. The samples with wicking normal to the fiber orientation (red curves in figure 11) display a slow increase in waterfront length which reaches its maximum at the end of the uptake, with the exception of more rapid increase at the onset for the 500 rpm membrane. The samples with wicking along the fiber direction (black curves in figure 11), show a strong increase of

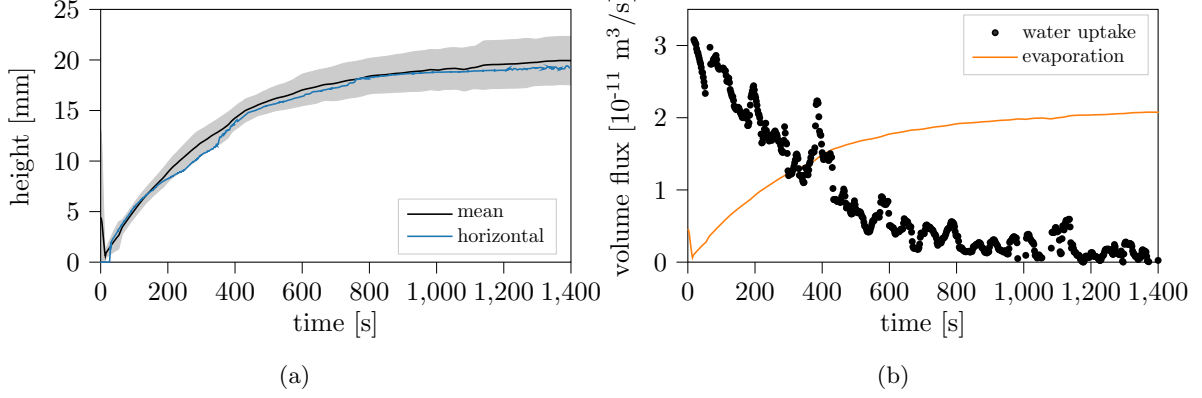


Figure 10: a) Mean front position for wicking in 1500 rpm membrane along fiber orientation. Black: average of samples from the 1500 rpm membrane (including horizontal), blue - horizontal experiment, b) Black: derivative of black curve in a) scaled with sample width and estimated membrane thickness, i.e. effective volume flux, orange: estimated evaporative losses at water film on membrane upstream from the front.

waterfront length starting at $t \approx 50$ s attributed to the formation of fingers and reaching the maximum waterfront length at $t \approx 400$ s. After that, the waterfront length decreases again for the samples with wicking along fiber orientation (figure 11b,c and d) reflecting the widening and merging of the initially sharp fingers (figure 8d-f). Actually, the waterfront length of wicking along fiber direction reaches up to four times the initial front length. Figures 12 and 13 are galleries of the waterfront shape of every sample at its maximal measured waterfront length for wicking along and normal to fiber orientation respectively. The samples in figure 12 with high drum rotation (>500 rpm) show prominent fingers pointing in the same direction as the wicking flow. Wicking normal to the fiber orientations for samples prepared from the same batch (figure 13 >500 rpm) also show fingers. However, they do not point sharply in wicking direction, but rather spread laterally as branches in the style of a pine tree (figure 8k and 13) and only appear late in the uptake process. The samples with low drum rotation or low degree of fiber orientation (500 rpm, figures 12 and 13) show fingers growing as wedges in apparently random directions, showing little difference between different fiber orientations.

4 Simulation results

Figure 14 and 15 compare the experimental and simulation results of uptake along fiber orientation. We study the influence of heterogeneity (with and without random field), i.e. p_{c0} as random field or constant, as well as the influence of capillary pressure increase due to waterfront gradient: local ($l_s = 1$) versus non-local ($l_s \geq 1$) approach. Figure 14 shows the results for the local approach ($l_s = 1$, deactivated increase due to waterfront gradient) for membranes without and with heterogeneity. For the homogeneous case (constant p_{c0}), a square root of time behavior as described by Lucas-Washburn is recovered. For the heterogeneous case, the uptake is faster than the for homogeneous case, but still slower than the experiment. The evolution of the waterfront is compared with the experimental results in figure 14b). Heterogeneity leads to an increasingly distorted waterfront, but no formation of fingers is observed as in the experiment.

Figure 15a) shows the non-local simulation ($l_s \geq 1$) results taking into account the increase of capillary pressure due to the waterfront gradient. Figure 4a) displays the random field with mean $p_{c0} = 136$ Pa and a deviation of maximal 10 Pa and high spatial correlation mimicking the fiber orientation. We note that evaporation, which has an increasing influence with time by enlarging the surface film area and results in higher absolute evaporative volume losses, is not included in our model. Therefore, we only consider the period until $t < 600$ s, which is also the crucial time span where fingers are formed. The waterfronts at selected time steps are displayed in figure 15b). Due to computational limitations a slender domain is simulated compared to the experimental one, but large enough to identify the trend of the wicking dynamics.

The wicking front dynamics show good agreement between simulation and experiment. While both simulation and experiment show an almost linear uptake behavior for early time, only the experimental curves ease off for $t > 400$ s because of evaporation. Qualitatively similar fingers appear and grow at

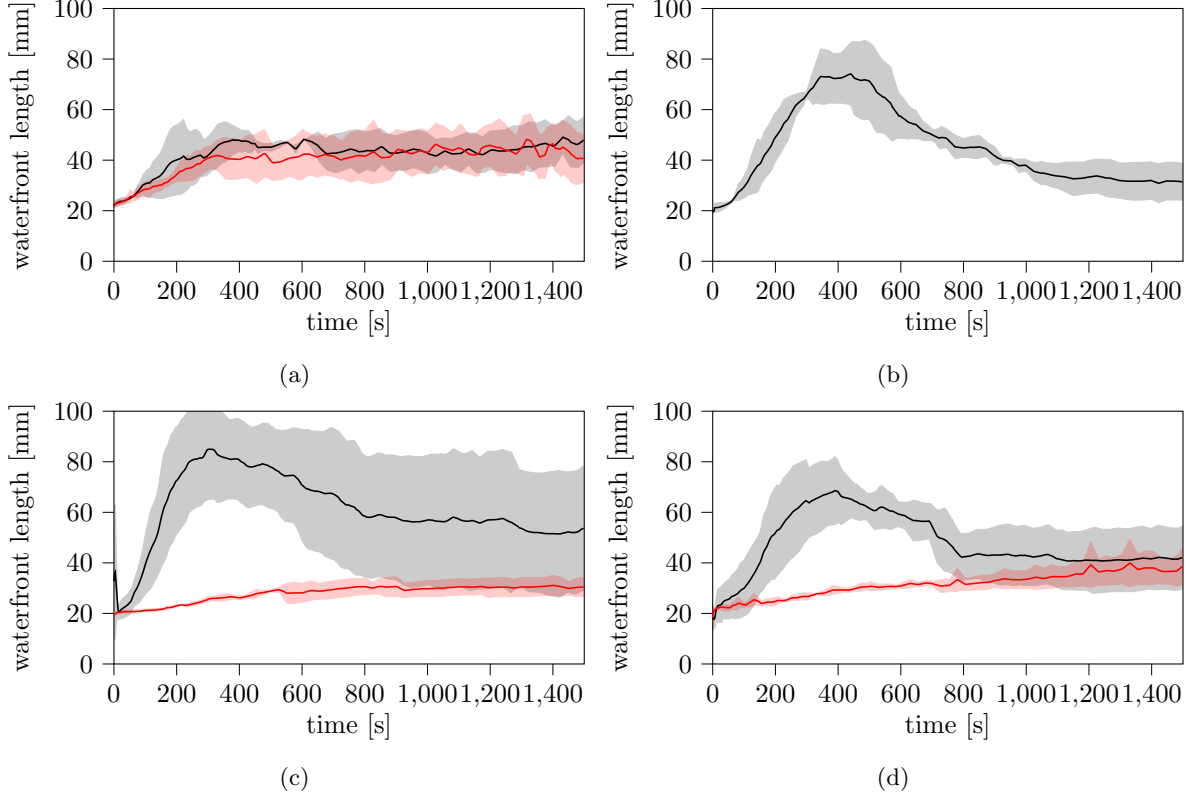


Figure 11: Average waterfront length (solid line) and standard deviation (light area) over time for samples taken from membranes produced with drum rotation a) 500 rpm, b) 1000 rpm, c) 1500 rpm and d) 2000 rpm. Black - fibers oriented along wicking direction; red - normal to wicking direction.

about the same time ($t \approx 130$ s) and position ($y \approx 2.5$ mm) in simulations and in experiment (figure 15). In figure 16, the results are presented for wicking normal to fiber direction by swapping the parameters σ_x and σ_y in the random field. The uptake dynamics show less agreement with experiments (figure 16a). The appearance of fingers in normal direction and the consequential formation of large wet knobs cannot be captured (figure 16b). The uptake dynamics and front shape deviate for later times. Table 1 lists the model parameters used in the simulation. Based on these values a parametric analysis is performed. Figure 17 shows the simulation results for two selected parametric sweeps of the model (see table 2) while keeping the other parameters as reported in table 1. Figure 17a shows the results for different noise levels indicating the level of heterogeneity. We observe that a minimum heterogeneity is required to trigger the formation of fingers, here at least a noise level of $\Delta_p = 0.9$. Simulations with low noise adhere to uptake in a homogeneous porous medium described by the Lucas-Washburn law, do not show fingers and have much slower uptake dynamics, while high noise runs show stronger finger formation and faster dynamics than the experiment. The mean capillary pressure is the same for all runs and due to the subsequent domain smoothing step, differences and absolute value of the variance are actually small (see table 2). On the other hand, heterogeneity alone is not sufficient to trigger the formation of fingers. Figure 17b shows that a minimum anisotropy and spatial correlation in capillary pressure is necessary to form fingers. Only runs with $\frac{\sigma_y}{\sigma_x} > 40$ show fingers in figure 17b. Figure 17c shows the waterfronets for the runs at $t = 145$ s, i.e. at the onset of fingering for the curves in figure 17a (left) and b (right). Not only is the uptake faster for higher noise levels and heterogeneity, also the fingers are longer already at the beginning of finger formation. The lateral location of the fingers is the same for all runs and depends on the underlying random field.

5 Discussion

The studied thin ENM show pronounced front fingering during wicking which is enhanced by a preferred fiber orientation. We suggest a perturbation in capillary pressure to be the origin of these wicking fingers followed by a non-local growth of fingers due to an increase in capillary pressure due to a non-

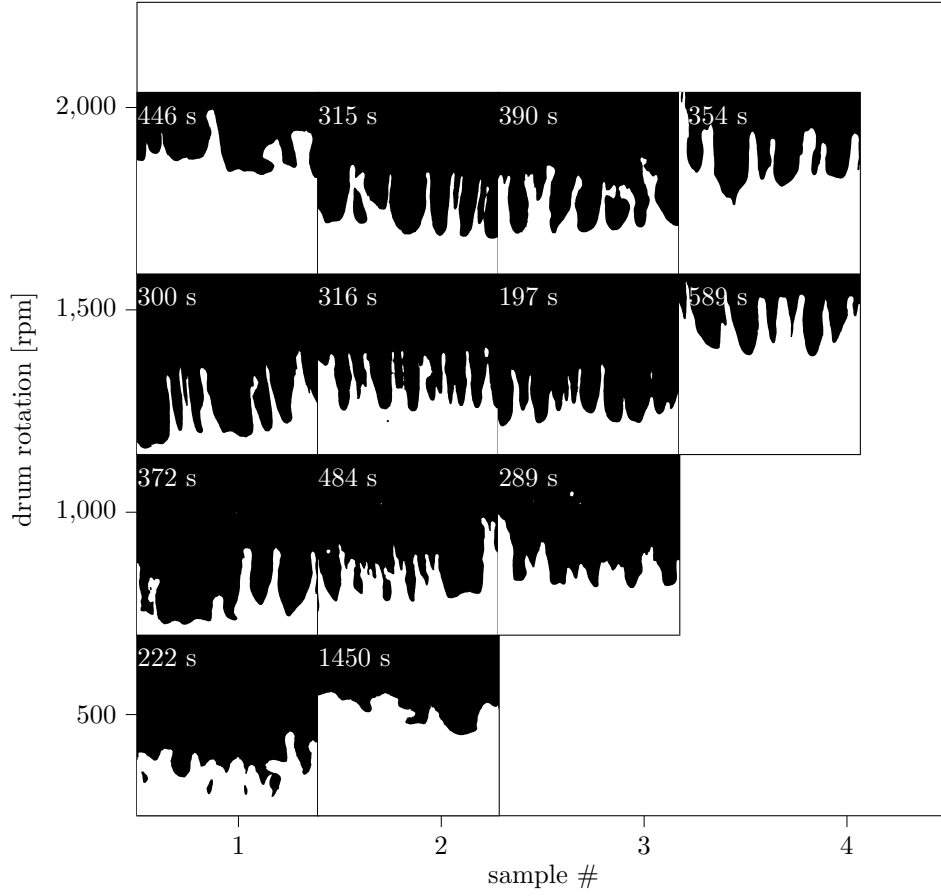


Figure 12: Waterfront shapes during wicking at maximal finger extension for flow along fiber orientation for different drum rotation, thus different fiber orientation.

Table 1: Parameters used in simulations.

symbol	description	value
b	membrane thickness	$30 \mu m$
	domain size y	$21.75^*/18^{**} mm$
	domain size x	$5.25^*/6.75^{**} mm$
Δ	grid element size	$75 \mu m$
g	gravitational acceleration	$9.81 \frac{N}{kg}$
ρ	water density	$1000 \frac{kg}{m^3}$
C	wicking constant	$0.475 \frac{mm}{\sqrt{s}}$
h_0	wicking height	$15 mm$
p_{c0}	derived base capillary pressure	$137.34 Pa$
	effective p_{c0} standard deviation	$2.29^*/4.65^{**} Pa$
σ_a	front smoothing length	$150 \mu m$
σ_c	waterfront correlation/smoothing length	$350 \mu m$
Δ_p	p_{c0} raw noise	1.25
σ_x	noise x correlation/smoothing length	$58.3 \mu m^*/3.5 mm^{**}$
σ_y	noise y correlation/smoothing length	$3.5 mm^*/58.3 \mu m^{**}$

*along fiber orientation, **normal to fiber orientation

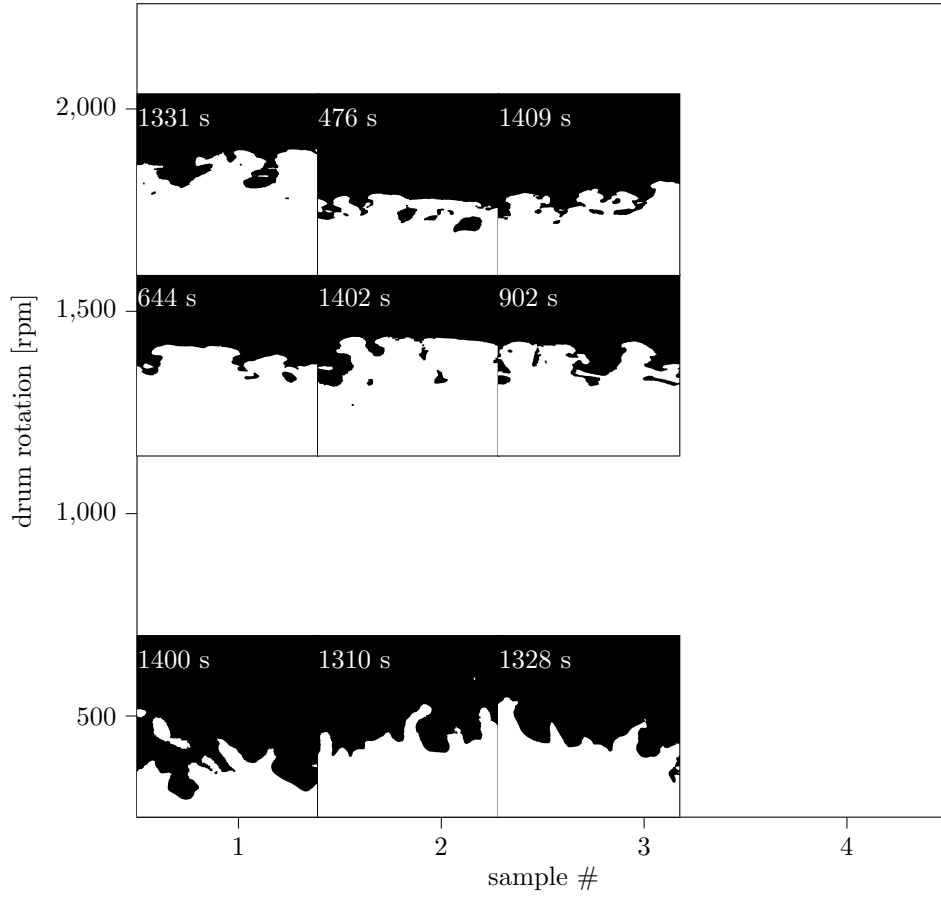


Figure 13: Waterfront shapes during wicking at maximal finger extension for flow normal to fiber orientation, for different drum rotation, thus different fiber orientation.

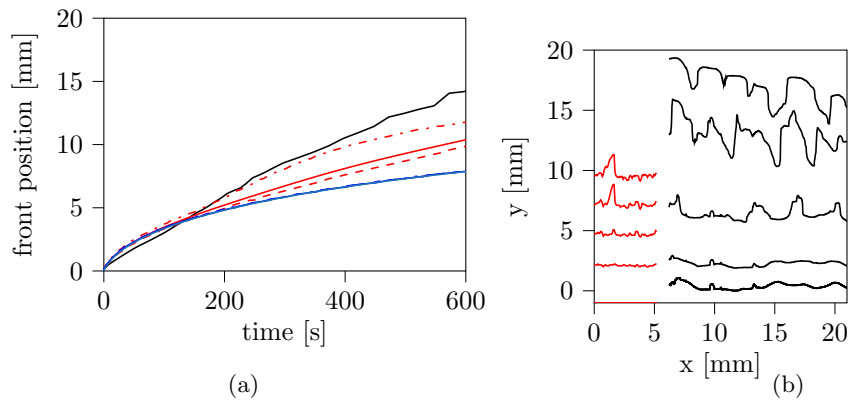


Figure 14: a) Comparison of simulation without capillary pressure increase to experimental uptake in fiber orientation calibrated for the cropped experimental images. black - one 1000 rpm sample, red - mean simulation front for domain with random field; dashed and dashed-dotted respective front minimum and maximum, blue - simulation front for domain without random field, with straight front and equivalent to Lucas-Washburn. b) comparison of waterfront shape evolution of heterogeneous (with random field) domain (red) to experiment (black).

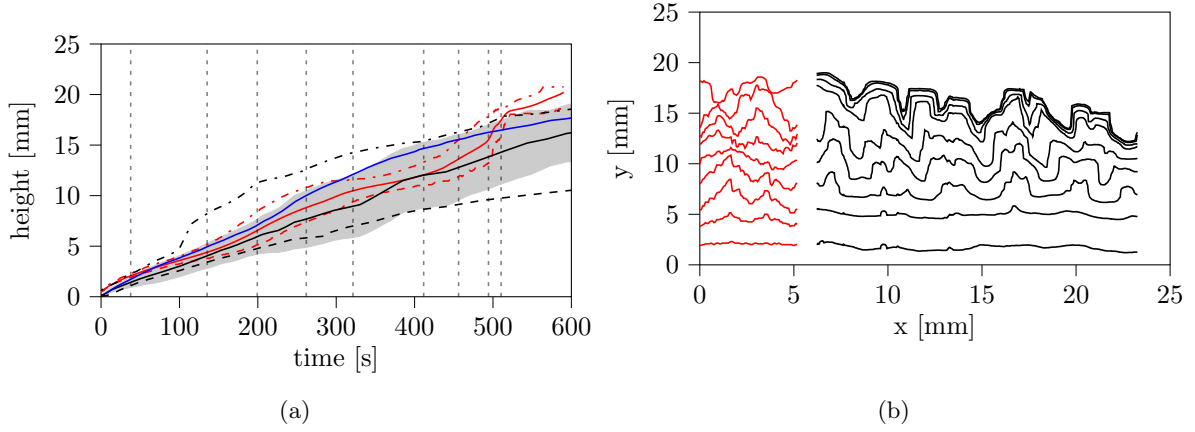


Figure 15: Wicking along fiber orientation. a) simulated waterfront position in red, dashed and dashed-dotted front minimum and maximum. black - median of waterfront positions of all 1000 rpm samples with standard deviation as gray area. Black dashed and dashed-dotted the respective medians of the front minima and maxima, blue - waterfront position of the 1000 rpm example shown in b). b) Waterfront of simulation (red) and experiment (black) at selected time steps marked in a).

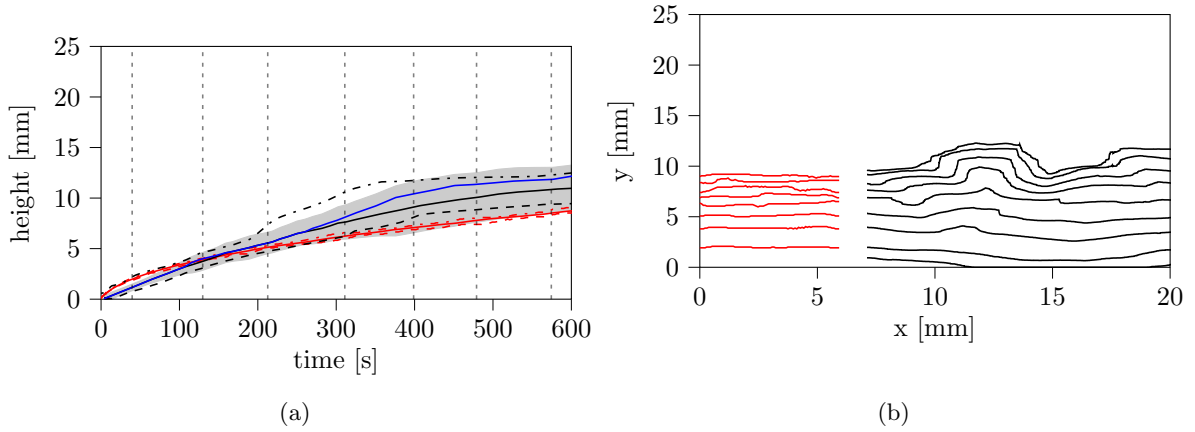


Figure 16: Wicking normal fiber orientation. a) simulated waterfront position in red, dashed and dashed-dotted front minimum and maximum. black - median of waterfront positions of all 2000 rpm samples with standard deviation as gray area. Black dashed and dashed-dotted the respective medians of the front minima and maxima, blue - waterfront position of the 2000 rpm example shown in b). b) Waterfront of simulation (red) and experiment (black) at selected time steps marked in a).

Table 2: Parametric sweeps and corresponding effective p_{c0} standard deviation.

noise	σ_x	$\frac{\sigma_y}{\sigma_x}$	p_{c0} standard deviation
0.3	58.3 μm	60	0.59 Pa (0.4%)
0.9	58.3 μm	60	1.77 Pa (1.3%)
1.1	58.3 μm	60	2.16 Pa (1.6%)
1.25	58.3 μm	60	2.45 Pa (1.8%)
1.4	58.3 μm	60	2.75 Pa (2.0%)
1.8	58.3 μm	60	3.50 Pa (2.5%)
1.25	175 μm	20	1.47 Pa (1.1%)
1.25	87.5 μm	40	2.01 Pa (1.5%)
1.25	58.3 μm	60	2.51 Pa (1.8%)
1.25	43.8 μm	80	2.92 Pa (2.1%)
1.25	35 μm	100	3.45 Pa (2.5%)

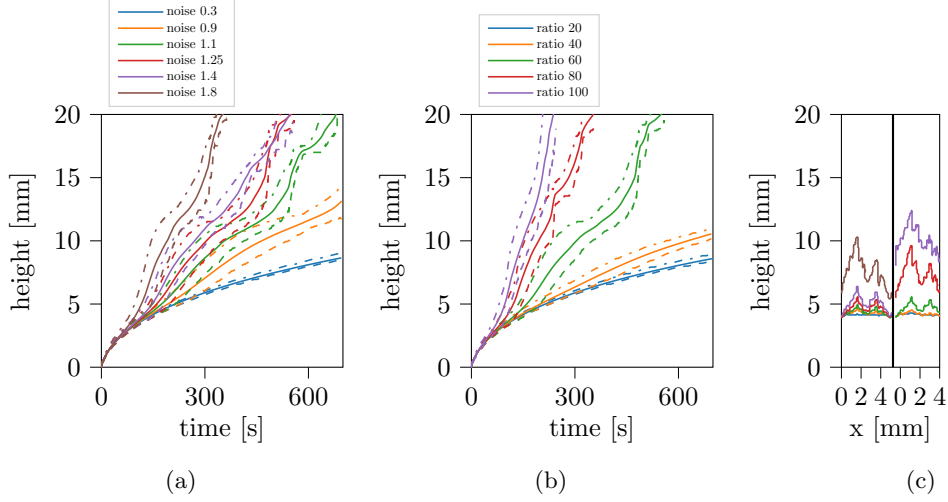


Figure 17: Wicking height (solid), base (dashed) and tips (dashed-dotted) versus time for a) simulations with varying noise parameter and b) simulations with varying p_{c0} correlation in x-direction. c) Waterfront at $t=145$ s: left-noise sweep, right - σ_x sweep. Noise 1.25 and ratio $\frac{\sigma_y}{\sigma_x} = 60$ are the experimentally matching simulation parameters.

linear waterfront. Section 2.5 derives the effect of the waterfront shape on the change of free energy for advancing the waterfront and consequently the capillary pressure. We could also interpret this as in the case of fingering the wetting process depends not only on the local value of the capillary pressure p_{c0} , but also on the gradient of the waterfront. Such an approach shows similarity to the gradient approach and in an integral formulation to the non-local approach, where the response at a certain point depends not only on the local value, but also on some information stemming from the neighborhood of this point [42].

The free energy evolution contains two variables, the wet surface and the water-air interface. Due to the small thickness of the membranes and the open pore space, the water-air interface formed by the thin film on the membrane surface strongly reduces the capillary pressure that would otherwise be expected for porous media with comparable void sizes. The uptake is consequentially much slower than predicted by the Lucas-Washburn model.

The continuity of the waterfront stretching over multiple inter-fiber voids, on the other side, gives rise to a non-local effect on the capillary pressure influenced by the waterfront shape described in equation (10). Waterfront locations with distorted front shape have more available solid surface area and can produce a stronger capillary suction than a straight front shape. Perturbations of the waterfront grow into fingers because the available fiber surface is larger than in the case of a straight front while the ratio of produced water-air interface to wetted solid surface stays constant.

The membranes appear rather homogeneous at the millimeter length scale and the SEM images give no indication of heterogeneity at the size of the formed fingers as for example observed in fractured porous media [23]. From experiments it is not clear what triggers the finger formation, but it is apparent that a spatial correlation and heterogeneity is required to trigger fingering and growth of fingers as shown by longer and sharper fingers for increased fiber orientation. Coincidentally highly aligned and close fibers will produce pathways that result in sharp membrane sections with locally increased capillary pressure instigating finger formation. Experimentally, the waterfront has a shape affected by features as small as fiber perimeters, which is currently unattainable for modeling. Section 2.6 describes a large scale model based on the balance of capillary pressure and viscous dissipation. Macroscopic material characteristics can be estimated by matching the early uptake phase, which displays its still straight waterfront, to the classic Lucas-Washburn model, e.g. the capillary pressure without increase of capillary pressure due to a non-linear waterfront.

The capillary pressure for the distorted waterfront is calculated from the front shape. We find good agreement of our proposed mechanism in the uptake dynamics and also the finger front characteristics. A drawback of the proposed model is that most model parameters are obtained from matching the simulation to the experimental observation and do not directly relate to actual microscopic parameters. Since the samples for wicking along and normal to fiber orientation are taken from the same membrane, there are no differences in macroscopic characteristics like porosity, pore size distribution or wettability,

yet the wicking dynamics differ strongly.

We attempt to reproduce this behavior with our model by varying the heterogeneity and anisotropy of the pore structure. Fingers appear only over a certain heterogeneity limit and concurrently a certain minimal spatial correlation to achieve a critical size of front perturbation. Similar to the experiment with increasing fiber alignment, fingering becomes more pronounced for stronger and more anisotropic imposed heterogeneity.

We believe that our model provides an explanation for the mechanism of wicking fingering in thin ENM. There are apparently several possible variables that could have additional qualitative and quantitative influences on the wicking fingering dynamics including fiber wettability, fiber thickness, fiber stiffness, membrane thickness and liquid viscosity. Further research is necessary to connect the variables assumed for the model to experimentally accessible membrane structure parameters. For example, while our model considers gravity because of the low estimated capillary pressure, the increase in capillary pressure due to fingers advances the front beyond the maximal uptake height h_0 , which corresponds to the limit of experimental uptake in normal orientation of fibers. While the experimental uptake limit appears as a reasonable value for h_0 and a suitable reference for the capillary pressure, the experimental uptake is clearly limited by evaporation and not by gravity.

6 Conclusion

We studied in-plane wicking in thin electrospun membranes of submicron sized EVOH fibers by back-light photography. The wicking dynamics is not only found to be much slower than expected for the predominant inter-fiber pore size, but also a pronounced waterfront fingering is observed with different front shapes and uptake dynamics by varying fiber alignment and orientation. We suggest a capillary pressure increase due to subtle waterfront perturbations caused by small anisotropic membrane heterogeneity trigger the onset of fingering. The perturbations grow into fingers because distorted front shapes produce stronger capillary pull than a straight front. A non-local control volume model considering the influence of the waterfront shape on the wicking process is developed to reproduce the experimentally observed water uptake. Despite the coarse length scale of the model compared to the membrane structure, good agreement is found for the finger formation and wicking dynamics. A potential approach for an improved model could be the employment of volume-of-fluid computational-fluid-dynamics, lattice-Boltzmann-method or level-set-method with the challenge to implement the non-local waterfront effect. Such an approach would still rely on fitting parameters, but would allow finer grids and help together with wider experimental parameter variation to identify or derive the underlying physical properties. Further improvement can be found in including evaporation into the model. Studying a wider range of experimental variables including batch-to-batch variation, membrane thickness, different liquids or polymers could allow to better understand the link between the microscopic membrane structure and macroscopic wicking dynamics.

Author Contributions (CRediT)

R. Fischer - Conceptualization, Formal analysis, Investigation, Methodology, Software, Validation, Visualization, Writing - original draft

J. Schoeller - Methodology, Resources, Writing - review & editing

R.M. Rossi - Conceptualization, Project administration, Supervision, Writing - review & editing

D. Derome - Conceptualization, Project administration, Supervision, Writing - review & editing

J. Carmeliet - Conceptualization, Project administration, Supervision, Writing - review & editing

S. Kunz - Resources

C. Schlepütz - Resources

Conflicts of interest

There are no conflicts to declare.

Acknowledgments

Stefan Kunz is gratefully acknowledged for help with the experimental setup. We further acknowledge the Paul Scherrer Institut, Villigen, Switzerland for provision of synchrotron radiation beamtime at the TOMCAT beamline X02DA of the SLS and Christian Schlepütz for the support during the beamtime.

A Appendix

A.1 Derivation of model conductivity

The conductivity g_{ij} is derived from Darcy's law and Washburn's law without gravity, taking as input the wicking constant C and the capillary pressure $p_{c0} = \rho gh_0$. Darcy's law is

$$p_c = RQ = khQ \quad (17)$$

where R is the flow resistance for a capillary of length h and k the length specific resistance factor. The flow rate Q can be written as the product of capillary cross-section area A and front velocity \dot{h} .

$$p_c = \rho gh_0 = khA\dot{h} \quad (18)$$

Solving the differential equation gives Washburn's law

$$h(t) = \sqrt{\frac{2\rho gh_0}{kA}t} = C\sqrt{t} \quad (19)$$

The cross-section area A is the product of the membrane thickness b and the element size Δ . The wicking constant C can be described by

$$C^2 = \frac{2\rho gh_0}{kb\Delta} \quad (20)$$

The base conductivity g_0 is the inverse base resistance between two fully wet elements.

$$g_0 = \frac{1}{k\Delta} = \frac{C^2b}{2\rho gh_0} \quad (21)$$

One element is connected to three elements of the next lower row in the grid: To one next neighbor and diagonally to two next nearest neighbors. The decreased conductivity of the diagonal elements is taken into account in the adjacency matrix with the value $\frac{1}{\sqrt{2}}$. g_0 has to be corrected by $1 + \sqrt{2}$ as the sum of the three connections and the degrees of saturation s of the elements i and j to yield the correct row-by-row conductivity described by the linear Washburn law giving the conductivity g_{ij} in equation (14)

$$g_{ij} = \frac{C^2b}{\rho gh_0} \frac{1}{(s_i + s_j) 1 + \sqrt{2}} \quad (22)$$

which recovers accurately Washburn's law for the homogeneous case (figure 14).

A.2 High-resolution X-ray tomographic microscopy

A small piece of membrane was examined with X-ray tomographic microscopy. A three millimeter wide strip is placed in a 5 mm wide tube on top of a rod with a short piece sticking out of the tube. The rod is placed on the rotating stage of the RX Solutions Easy Tom XL and the field of view focused on the small piece. The voxel size is $0.52 \mu\text{m}$. A representative slice and a 3D rendering are shown in figure 18. The membrane has a thickness of around $30 \mu\text{m}$, yet not perfectly uniform. Despite strong local tomography and ring artifacts, the membrane can be resolved, but not the composing fibers.

A.3 Time-resolved X-ray tomographic microscopy

During the experimental campaign in [29], a narrow (3 mm) strip of ENM was placed in the sample holder and wicking recorded with the same setting at one full tomographic scan per second. The narrow strip leads to folding at the edges when wetted and the mounting cannot prevent movement of the sample. Consequently, only a few scans provide useful qualitative data during early wicking showing only a small

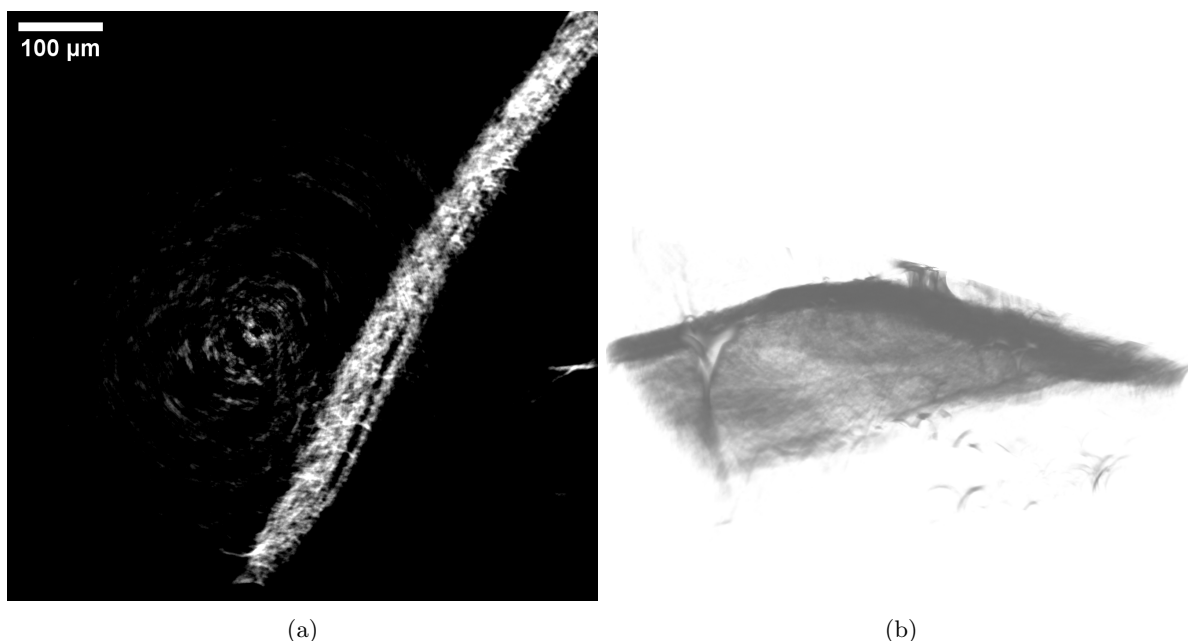


Figure 18: a) tomographic slice (white) and b) 3D visualization of X-ray tomographic microscopy of membrane with voxel size $0.52\ \mu\text{m}$.

part of the sample. Figure 19 shows a selected scan during water rise in the membrane. The voxel size is $2.75\ \mu\text{m}$ and the sub-micron fibers show too little absorption to be resolved. However, water filling the inter-fiber void space and forming a thin film on the membrane surface can be observed shown as solid gray wedge in figure 19. The waterfront is straight in trans-membrane direction confirming the quasi-2D approach presented in this work.

References

- [1] L. Weidenbacher, A. Abrishamkar, M. Rottmar, A.G. Guex, K. Maniura-Weber, A.J. deMello, S.J. Ferguson, R.M. Rossi, G. Fortunato, *Acta Biomater* **64**, 137 (2017). DOI 10.1016/j.actbio.2017.10.012
- [2] R.S. Bradley, I.K. Robinson, M. Yusuf, *Macromol Biosci* **17**(2) (2017). DOI 10.1002/mabi.201600236
- [3] K. Lee, S. Lee, *Fibers and Polymers* **21**(5), 999 (2020). DOI 10.1007/s12221-020-9300-6
- [4] R. Innocenti Malini, J. Lesage, C. Toncelli, G. Fortunato, R.M. Rossi, F. Spano, *European Polymer Journal* **110**, 276 (2019). DOI 10.1016/j.eurpolymj.2018.11.017
- [5] J. Schoeller, F. Itel, K. Wuertz-Kozak, S. Gaiser, N. Luisier, D. Hegemann, S.J. Ferguson, G. Fortunato, R.M. Rossi, *Nanomaterials (Basel)* **11**(7) (2021). DOI 10.3390/nano11071850
- [6] B. Singh, K. Kim, M.H. Park, *Nanomaterials (Basel)* **11**(12) (2021). DOI 10.3390/nano11123411
- [7] T. Lu, J. Cui, Q. Qu, Y. Wang, J. Zhang, R. Xiong, W. Ma, C. Huang, *ACS Appl Mater Interfaces* **13**(20), 23293 (2021). DOI 10.1021/acsami.1c06520
- [8] M. Zhu, J. Han, F. Wang, W. Shao, R. Xiong, Q. Zhang, H. Pan, Y. Yang, S.K. Samal, F. Zhang, C. Huang, *Macromolecular Materials and Engineering* **302**(1) (2017). DOI 10.1002/mame.201600353
- [9] Y. Dong, J. Kong, S.L. Phua, C. Zhao, N.L. Thomas, X. Lu, *ACS Appl Mater Interfaces* **6**(16), 14087 (2014). DOI 10.1021/am503417w
- [10] Y. Dong, J. Kong, C. Mu, C. Zhao, N.L. Thomas, X. Lu, *Materials Design* **88**, 82 (2015). DOI 10.1016/j.matdes.2015.08.107

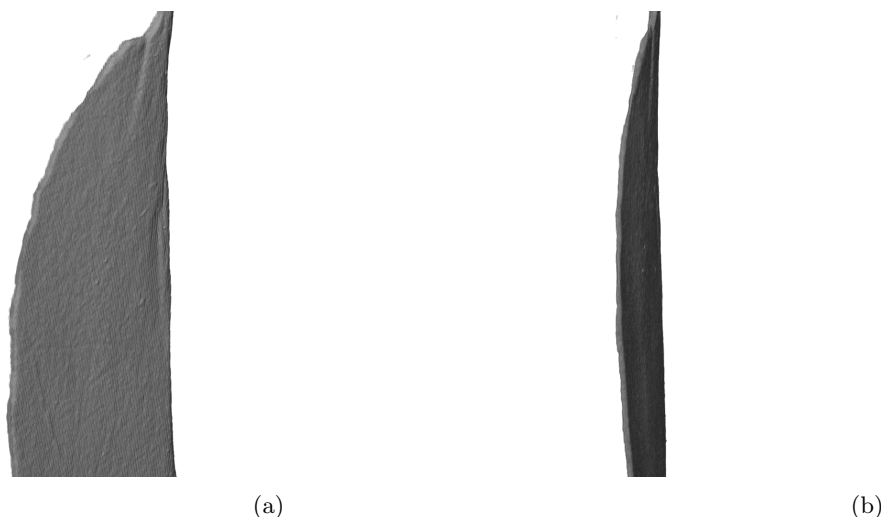


Figure 19: 3D visualization of water for two viewpoints at selected time step as obtained from time-resolved XTM with voxel size $2.75\ \mu\text{m}$. Displayed height 4 mm.

- [11] Y. Zhang, T.T. Li, H.T. Ren, F. Sun, Q. Lin, J.H. Lin, C.W. Lou, *RSC Advances* **10**(6), 3529 (2020). DOI 10.1039/c9ra06022g
- [12] S. Chevalier, N. Lavielle, B.D. Hatton, A. Bazylak, *Journal of Power Sources* **352**, 272 (2017). DOI 10.1016/j.jpowsour.2017.03.098
- [13] R. Sood, S. Cavaliere, D.J. Jones, J. Rozière, *Nano Energy* **26**, 729 (2016). DOI 10.1016/j.nanoen.2016.06.027
- [14] T. Agaesse, A. Lamibrac, F.N. Büchi, J. Pauchet, M. Prat, *Journal of Power Sources* **331**, 462 (2016). DOI 10.1016/j.jpowsour.2016.09.076
- [15] M. Parada, D. Derome, R.M. Rossi, J. Carmeliet, *Textile Research Journal* **87**(1), 110 (2017). DOI 10.1177/0040517515622151
- [16] T. Bultreys, W. De Boever, V. Cnudde, *Earth-Science Reviews* **155**, 93 (2016). DOI 10.1016/j.earscirev.2016.02.001
- [17] S. Domaschke, A. Morel, R. Kaufmann, J. Hofmann, R.M. Rossi, E. Mazza, G. Fortunato, A.E. Ehret, *J Mech Behav Biomed Mater* **104**, 103634 (2020). DOI 10.1016/j.jmbbm.2020.103634
- [18] B. Bijeljic, B. Markicevic, H.K. Navaz, *Phys Rev E Stat Nonlin Soft Matter Phys* **83**(5 Pt 2), 056310 (2011). DOI 10.1103/PhysRevE.83.056310
- [19] J. Zhao, F. Qin, D. Derome, J. Carmeliet, *Journal of Hydrology* **588** (2020). DOI 10.1016/j.jhydrol.2020.125080
- [20] E.P. Montellá, C. Yuan, B. Chareyre, A. Gens, *Advances in Water Resources* **144** (2020). DOI 10.1016/j.advwatres.2020.103709
- [21] A. Rabbani, M. Babaei, *Advances in Water Resources* **126**, 116 (2019). DOI 10.1016/j.advwatres.2019.02.012
- [22] A. Kubilay, A. Ferrari, D. Derome, J. Carmeliet, *Journal of Building Physics* **45**(1), 36 (2020). DOI 10.1177/1744259120968586
- [23] S. Roels, K. Vandersteen, J. Carmeliet, *Advances in Water Resources* **26**(3), 237 (2003). DOI 10.1016/s0309-1708(02)00185-9
- [24] L. Wang, H.B. Huang, X.Y. Lu, *Phys Rev E Stat Nonlin Soft Matter Phys* **87**(1), 013301 (2013). DOI 10.1103/PhysRevE.87.013301

- [25] F. Qin, J. Zhao, Q. Kang, D. Derome, J. Carmeliet, *Transp Porous Media* **140**(1), 395 (2021). DOI 10.1007/s11242-021-01644-9
- [26] L. Courbin, J.C. Bird, M. Reyssat, H.A. Stone, *J Phys Condens Matter* **21**(46), 464127 (2009). DOI 10.1088/0953-8984/21/46/464127
- [27] M. Reyssat, L. Courbin, E. Reyssat, H.A. Stone, *Journal of Fluid Mechanics* **615**, 335 (2008). DOI 10.1017/s0022112008003996
- [28] A. Ferrari, I. Lunati, *Advances in Water Resources* **74**, 1 (2014). DOI 10.1016/j.advwatres.2014.07.009
- [29] R. Fischer, C.M. Schlepütz, D. Hegemann, R.M. Rossi, D. Derome, J. Carmeliet, *Physical Review E* **103**(5) (2021). DOI 10.1103/PhysRevE.103.053101
- [30] R. Fischer, P. Boillat, L. Weidenbacher, D. Derome, R.M. Rossi, J. Carmeliet, *Proceedings of the 19th World Textile Conference - Autex 2019* (2019)
- [31] Z. Püspöki, M. Storath, D. Sage, M. Unser, *Focus on Bio-Image Informatics* **219**, 69 (2016). DOI 10.1007/978-3-319-28549-8_3
- [32] J. Schindelin, I. Arganda-Carreras, E. Frise, V. Kaynig, M. Longair, T. Pietzsch, S. Preibisch, C. Rueden, S. Saalfeld, B. Schmid, J.Y. Tinevez, D.J. White, V. Hartenstein, K. Eliceiri, P. Tomancak, A. Cardona, *Nat Methods* **9**(7), 676 (2012). DOI 10.1038/nmeth.2019
- [33] J.M. Bell, F.K. Cameron, *The Journal of Physical Chemistry* **10**(8), 658 (1906). DOI 10.1021/j150080a005
- [34] R. Lucas, *Kolloid-Zeitschrift* **23**(1), 15 (1918). DOI 10.1007/BF01461107
- [35] E.W. Washburn, *Physical Review* **17**(3), 273 (1921). DOI 10.1103/PhysRev.17.273
- [36] D. Quéré, *Europhysics Letters (EPL)* **39**(5), 533 (1997). DOI 10.1209/epl/i1997-00389-2
- [37] R. Lenormand, E. Touboul, C. Zarcone, *Journal of Fluid Mechanics* **189**(-1) (1988). DOI 10.1017/s0022112088000953
- [38] R. Lenormand, C. Zarcone, *Transport in Porous Media* **4**(6), 599 (1989)
- [39] B.K. Primkulov, A.A. Pahlavan, X. Fu, B. Zhao, C.W. MacMinn, R. Juanes, *Journal of Fluid Mechanics* **923** (2021). DOI 10.1017/jfm.2021.579
- [40] S.M. Troian, E. Herbolzheimer, S.A. Safran, J.F. Joanny, *Europhysics Letters (EPL)* **10**(1), 25 (1989). DOI 10.1209/0295-5075/10/1/005
- [41] J.R. de Bruyn, *Phys Rev A* **46**(8), R4500 (1992). DOI 10.1103/physreva.46.r4500
- [42] E. Benvenuti, A. Simone, *Mechanics Research Communications* **48**, 46 (2013). DOI 10.1016/j.mechrescom.2012.12.001